Supporting Information

Szpankowski et al. 10.1073/pnas.1120510109

SI Text

Uncertainty in Subpixel Localization and Intensity Measurements. We conducted an analysis of the uncertainty in position and intensity measurements in the context of the biological application. For each detected feature in a given channel, the Gaussian-fitting algorithm implemented in this study determines a measure of uncertainty in the *x*-coordinate, *y*-coordinate, and in the case of amplitude intensity measurements, a goodness-of-fit. Positional accuracy is mainly influenced by two factors; the signal-to-noise ratio (SNR) and the point to point-to-point distance. To address the influence of the SNR, simulations on isolated spots were previously performed and confirm that center positions of features with a known intensity distribution, in this case the distribution of the point-spread function (PSF), can be determined with sub–20-nm precision (1, 2). For applications with a high SNR, the precision reached the single nanometer range. The practical uncertainty in positional estimates in both the *x*- and *y*-coordinates for the amyloid precursor protein (APP) anchor channel is presented for six randomly selected images from six control animals (Fig. S1). The average uncertainty for *x* and *y* was determined to be 29.6 nm and 29.9 nm, respectively. Hence, with an established threshold of 300 nm for each colocalization event, features were detected with ∼90% accuracy. Additionally, 92.6% of the position data had an uncertainty of less than 60 nm, or ∼20% uncertainty. For the same test set, an average intensity amplitude uncertainty of 7.2% was observed based on the goodness-of-fit for each detected point source fit by a Gaussian function. Overall, the position and intensity measurements reported in this study were determined to fall within an acceptable accuracy for the desired application.

Comparison with Superresolution Microscopy. The subpixel detection accuracy of fluorescent puncta was confirmed by directly comparing Gaussian fitting of conventional microscopy data analyzed in this study to superresolution imaging. Our results indicated that the subpixel localization method we implemented predicts coordinates of detected puncta accurately compared with structured illumination-based OMX (Applied Precision Instruments) superresolution analysis of the same data. As a test case, we used a small sample of neurons stained with the early endosome marker Rab5, which produced vesicular staining patterns similar to what we observed with APP and the motor subunits light chain of kinesin-1 (KLC1) and heavy chain of cytoplasmic dynein (DHC1). We observed 96.05 ± 1.42% (three images, 918 detected features) of puncta detected through conventional microscopy colocalized with puncta in analogous images acquired using OMX. The average distance of colocalization between determined subpixel positions for a given feature obtained from conventional microscopy compared with its higher-resolution counterpart acquired through OMX was 32.6 nm, or roughly equivalent to the localization error. In addition, 83.2 ± 2.6% (three images, 957 detected features) of puncta detected in OMX images colocalized with conventional microscopy features averaging 39.3 nm of spatial separation. In both cases, a correlation of $r = 0.89$ was observed between associated intensity values.

KLC1-Dependent DHC1 Association with APP Vesicles. Our results indicate that APP recruits DHC1 (Figs. 3*C* and 4*A*) and that levels of this dynein subunit depend on KLC1 amount on the vesicle (Fig. 5*A*), thus suggesting a mechanism that can explain earlier reports showing that reducing kinesin-1 function results in retrograde impairment (3–7). We propose three simple hypotheses to account for these observations, which we are now able to distinguish with our method and resulting data. The first theory is an "activation" hypothesis, which states that kinesin-1 activates dynein on the vesicle; hence, reductions in kinesin-1 impair retrograde transport by decreasing activation of dynein subunits on cargo surfaces. The second theory is an "association-impairment" hypothesis, which posits that kinesin-1 is required for proper association of dynein on APP vesicles and that loss of kinesin-1 on cargo leads to reduced dynein on vesicles. Third, the "sampling bias" hypothesis suggests that only vesicles with kinesin-1 activity in excess of dynein activity can enter and remain in an axon. Thus, when kinesin-1 levels are reduced and the relative amount of dynein on each vesicle increases, vesicles with low kinesin-1 to dynein ratios preferentially return to the cell body and ultimately do not pass through regions where transport is typically imaged. In this scenario, the prediction is that the number of moving vesicles in distal regions of the axon will significantly decrease after reduction of kinesin-1. In fact, this observation was reported for APP vesicles in *Drosophila* axons lacking one copy of kinesin-1 (8), an effect that no other motor subunit mutant displayed, suggesting that a sampling bias may exist in distal regions of the axon.

Our findings show significant reductions of DHC1 subunit association and relative amount as a function of decreasing KLC1 copy number. These observations best support the association-impairment hypothesis, but do not rule out the possible additional contribution of a sampling bias. To test for a sampling bias in our data, axonal regions need to ideally be imaged at set locations, where motor composition of APP vesicles as a function of distance from the cell body can be determined. We were unable to obtain such data because of the complex meshwork of projections in these cultures where axons often bifurcate and fasciculate. However, because the sampling-bias theory was first established based on the observation that the number of moving particles in distal axonal regions in kinesin-1 mutants were significantly reduced compared with all other genotypes, determining the number of detected APP vesicles as a function of *KLC1* gene dose can help distinguish between the remaining hypotheses. Although the immunofluorescence data used for motor localization cannot differentiate between moving and stationary particles, we do not see any difference in the number of detected APP vesicles as a function of KLC1 amount (Fig. S8). We observed ∼1 APP vesicle per micrometer of axon for each *KLC1* genotype, This result suggests that a sampling bias was not present in our data, because the same number of APP features were found on average in each randomly located region of the axon irrelevant of the amount of KLC1 or DHC1 present on APP vesicles. Taken together, our observations support the association-impairment hypothesis, where KLC1 is necessary for proper association of the motor subunit DHC1 onto APP vesicles and can explain, at least in part, why retrograde defects are observed in kinesin-1–deficient systems.

Future Considerations. Future investigations aimed at drawing conclusions about the motile state of APP-containing vesicles will require a combination of approaches. Although the goal of this study was to rigorously determine motor subunit association with endogenous APP vesicles, the power of the proposed method is being applied to ongoing investigations into the motor recruitment of fluorescently tagged APP vesicles in APP mutant contexts, where a variety of transport defects have been identified (9). Moreover, previous work using a hybrid approach of

live-imaging followed by quantitative immunofluorescence led to a robust analysis of motor composition on exogenous cargos that have been tracked and classified as stationary, anterograde, retrograde, or reversing (5). Although technically challenging, this approach provides unique insight into cargo movement features. However, these immunofluorescence applications alone cannot distinguish active motors from inactive motors, a measurement that traditionally requires the use of optical traps and force measurements (10, 11) not yet amenable to studying cargos from intact axons.

There is a possibility that the antibodies used in this study may not detect all APP, kinesin-1, and dynein because of subsets of feature that remain below threshold detection or are subject to steric hindrance and masking of epitopes. In particular, the antibody used to detect APP is monoclonal and directed to a region that is heavily implicated in APP interactions with other proteins. In cases where these endogenous APP binding partners mask the single epitope detected by the antibody, chances of detecting that particular APP molecule can be significantly thwarted. If this issue affects all of the genotypes analyzed in this study equally, the relative comparisons from which our conclusions were drawn remain robust. As is the case with most methods, the full picture will be unraveled from a combination of approaches including immunocytochemistry and heterologous expression of proteins tagged with small, nondisruptive tags that avoid issues with steric hindrance and epitope masking.

Previous methods aimed at addressing how APP interacts with endogenous proteins through colocalization analyses (12, 13) were informative, but did not directly focus on investigating motor subunit composition of vesicles. Our method relies on the highly improved resolution of endogenous protein colocalization, careful validation, and robust quantification of detected feature intensity in high-throughput. In summary, the subpixel colocalization method we describe has allowed us to assess relative motor subunit amounts on APP vesicles, test key predictions of APP's role in motor recruitment, and propose novel features of vesicle transport regulation in axons that were previously unapproachable. Taken together, our findings suggest that the amount of APP in vesicles controls the amount of KLC1 recruited to the vesicle surface. Moreover, it seems that levels of both APP and KLC1 play a role in proper recruitment and loading of DHC1 to APP axonal vesicles. From these data, it is difficult to definitively establish whether APP or KLC1 amount is the primary component responsible for the recruitment of dynein heavy chain to the vesicle. This important feature of APP motor composition regulation will require further examination.

SI Materials and Methods

Mice and Cell Culture. Mice used throughout this study were in the C57BL/6 background. *KLC1* and *APP* mice were described previously (14, 15). Pups were collected on the day they were born [or through caesarean section on embryonic days 19–20 in the case of *KLC1* mutants, as most die shortly after birth]. Hippocampal cells were dissociated and plated following a protocol described in ref. 16. Briefly, whole brains were dissected and hippocampi were extracted in cold Hank's buffer solution (500 mL HBSS, 0.4 g D-glucose, 0.834 g Hepes, 5 mL pen-strep, filter sterilized and set to pH 7.3). Cells were dissociated through manual trituration following 20-min incubation with the cysteine protease papain (Worthington) at 37 °C. Cells were then plated on cover-slips treated with poly-Lysine (Invitrogen), and left to adhere to the glass in DMEM (Invitrogen) + 10% FBS media. After 1 h, DMEM + FBS was removed, and cells were plated in optimal growth media [49 mL Neurobasal-A (Invitrogen), 130 μL glutamax (Invitrogen), 1 mL B27] in which they were allowed to grow at 37 °C and 5.5% CO_2 for 10 d.

Transfections. Transfection of hippocampal cells was carried out on day 9 using Lipofectamine 2000 (Invitrogen). All immunofluorescence for transfected cells was performed on day 10. The APP-YFP construct was designed and characterized as in ref. 17. KLC2 and DHC1 shRNA constructs were previously built as part of a kinesin and dynein lentiviral minilibrary, in a pLL3.7 GW lentiviral vector with gateway entry modifications and a mCherry marker (5).

Immunofluorescence and Microscopy. Antibodies used to probe desired motor protein subunits and APP were carefully selected and thoroughly tested to provide a reproducible assay as determined by quantitative image analysis. The following primary antibodies were selected for motor colocalization immunofluorescence experiments: anti-Alzheimer precursor protein (APP; Millipore C-term Jonas; MAB343, mouse monoclonal IgG), anti-kinesin light chain 1 (KLC1; Santa Cruz V-17, sc-13362, goat polyclonal IgG), and anti-dynein heavy chain (DHC1; Santa Cruz R-325, sc-9115, rabbit polyclonal IgG). Corresponding secondary donkey anti-mouse (Alexa Fluor 488), donkey anti-goat (Alexa Fluor 647), and donkey anti-rabbit (Alexa Fluor 568) antibodies were respectively chosen to minimize emission overlap and maximize signal. All secondary antibodies were raised in donkey to minimize cross-reactivity (see *Antibody Validation*, below). Cells were fixed with 4% paraformaldehyde plus 4% glucose for 30 min at 37 °C and 5.5% CO_2. Fixed cells were subsequently incubated for 5 min at room temperature with 0.1% Triton X-100 (TX-100) for permeabilization, followed by a 45-min incubation in blocking agent consisting of 10% donkey serum, 3% BSA, 0.1% TX-100 in PBS. Cover-slips were incubated with primary antibodies overnight at 4 °C, washed four times with PBS for 5 min, then incubated with secondary antibodies for 1 h at room temperature. Cells were washed four additional times with PBS at room temperature to remove all unbound secondary and then mounted on slides using ∼1.5 μL of ProLong Gold (Invitrogen), an antifade reagent that suppresses photobleaching and preserves the signal of fluorescently labeled target molecules. Slides were left to dry for 1 h, then sealed with standard nail polish.

Images were acquired at 100× with a 1.4 NA oil objective using a Deltavision RT deconvolution imaging system (Applied Precision Instruments). Image analysis efforts using a similar Deltavision deconvolution imaging setup resulted in a quantitative analysis of autophagy-related protein stoichiometry (18). Olympus immersion oil (n = 1.5180) was selected based on the mounting media used and sample/cover-slip thickness.

The particular antibodies selected provided the cleanest and most reliable imaging data. Serial antibody dilutions were used to elucidate appropriate primary concentrations that sufficiently saturated the sample while minimizing background signal. The resulting intensity profiles from each dilution were analyzed and primary antibody concentrations of 1:100 for all three antibodies were selected. Once primary antibody concentrations were determined, a similar approach was used to determine optimal secondary dilutions. A concentration of 1:200 sufficiently saturated the sample and was used for all subsequent experiments.

Axons were distinguished from dendritic projections by morphology and traced back to the cell body when possible. Care was taken to ensure axonal projections were well-isolated from adjacent features and spanned the field of view (67.9 μm) in one optical section, remaining entirely in focus. Image capture was done with a 12-bit CoolSnap HQ cooled CCD camera resulting in 512 × 512 images and a pixel size of 132.6 nm/pixel. Optical sections were spaced 300-nm apart in each of the three channels, reaching the diffraction limit in the z-plane. Exposure times for each channel (FITC – APP; Cy-5 – KLC1; Texas Red – DHC1) were empirically determined at the beginning of each series of experiments, by determining the saturation point and scaling exposure to a level

~30% below, leaving room for future samples containing features with higher intensity profiles. Once settings were established, they were kept constant throughout data collection.

Intensity Normalization Approach. Ideally, all imaging for a particular experiment was performed on the same day to control for the age and corresponding intensity variability of the mercury light source. Indeed, in many cases, a continuous imaging session was sufficient to collect all of the desired immunofluorescence data for a given experiment, but comparison of intensity profiles between images collected on separate days was problematic. To control for this inevitable variation, a normalization method was developed to facilitate comparison between samples from experiment to experiment. Molecular Probes offers a microscope image-intensity calibration kit that has proven to be instrumental for quantitative image analysis applications (19). The calibration kit includes 2.5-μm diameter InSpeck beads that correspond to commonly used emission/excitation spectra. Beads corresponding to FITC, Cy-5, and Tx-Rd channels were selected to evaluate the reproducibility of fluorescence intensity measurements from APP, KLC1, and DHC1, respectively, when acquisitions were performed under various conditions and on different days. Extensive analysis of the InSpeck beads showed that: (*i*) standardization was possible, (*ii*) accurate and reliable fluorescence measurements could be obtained, and (*iii*) specimens showing large differences in fluorescence intensity could be objectively compared (19). These beads exhibited minimal bleaching and slides prepared with these calibration standards were reused for a period of 3 mo. All beads were mounted on slides using ~1.5 μL of ProLong Gold antifade reagent.

InSpeck beads were imaged at the beginning and end of an imaging session. Three images were collected for each channel before and after image acquisition, and pooled to provide a measure of bulb intensity for a given day. When comparing between two datasets, sample intensity values were scaled according to the corresponding InSpeck profiles, allowing for reliable comparison of intensity values. Besides the primary function of providing a normalization scheme to compare quantitative intensity measurements between different imaging events, the beads were also used to evaluate the integrity of images acquired for a particular channel on a given day. For example, because these beads are uniform in intensity, one can confirm that the entire image is being collected with an unvarying degree of intensity.

Pixel Registration Correction. For diffraction limited systems in particular, chromatic aberration of the fluorescent channels can complicate analysis especially when efforts are being made to precisely detect positions of desired puncta. Additionally, because each channel is collected using a different wavelength, these small differences can lead to shifts in the true position of features. Daily calibration and instrumentation adjustments are required for high-precision imaging of fluorescent probes. To account for these wavelength shifts, the pixel data from each channel and optical section were corrected for all three planes (*x*-*y*-*z*). TetraSpeck (Invitrogen) microspheres are useful for verifying the ability of instrumentation to colocalize and resolve objects emitting different wavelengths of light in the same optical plane. The microspheres used were stained with different fluorescent dyes, which display four well-separated excitation/emission peaks: 365/430 nm (blue), 505/515 nm (green), 560/580 nm (orange), and 660/680 nm (dark red). Beads are available in five diameters, spanning the range from subresolution to nearly cell-sized particles. To calibrate the instrument and determine settings, 0.5-μm TetraSpeck beads were selected, diluted to a concentration of ~15,000 particles per microliter, and mounted on slides using ProLong Gold medium. Two images, capturing ~30 beads on average, were collected before any given imaging session using the 100× 1.4 NA DeltaVision objective. TetraSpeck calibration is required for each objective, established settings, and instrumentation used.

The automated pixel registration correction function available in the Volocity imaging software suite (Perkin-Elmer) was used to correct for chromatic aberration and wavelength shifts of desired fluorophores in 3D. Optical stacks containing the TetraSpeck calibration beads were input, and the software provided optimal registration correction. Images were corrected by an upward shift of one optical plane in the A568 (DHC1) channel and no shifts in the *x*-*y* plane (Fig. S2). This correction was applied to all images in a series for each experiment before image analysis.

Additionally, registration issues were addressed in the context of a specific sample as opposed to an "ideal" sample, such as the synthetic microspheres. Hippocampal cells were stained with anti-APP primary followed by a mixture of different color secondaries (donkey anti-mouse 488, goat anti-mouse 568, rabbit anti-mouse 647) corresponding to the APP mouse antibody. This process effectively marked the same APP positions and intensities in the three channels corresponding to the aforementioned schema. Pearson correlation coefficients were calculated for intensity data from selected axonal projections in the resulting images using a manually annotated line scan. The correlation coefficient significantly increased from $r = 0.81$ in uncorrected images to $r = 0.92$ when a *z*-shift of +1 in the A568 channel was incorporated. This one frame-shift is reproducible for the given objective using both ideal and specific samples and was used for the preprocessing of images before each experimental analysis.

Antibody Validation. The analysis of immunofluorescence data can only be as reliable as the images that are used. It is imperative that the antibodies selected and described above to detect position and intensity information are specific to their designated targets. Validation of primary and secondary antibody combinations against APP, KLC1, and DHC1 was conducted to achieve specificity, reproducibility, sample saturation, and minimal cross-reactivity and background noise. Because *DHC1*$^{-/-}$ mice are unavailable, the DHC1 primary antibody was tested in DHC1 shRNA-transfected hippocampal cells. Validation of shRNA constructs for reduction of DHC1 was done by transfecting N2a cells separately with three sequences of each target using Lipofectamine 2000 (Invitrogen). Quantitative PCR was performed to test for reduced mRNA expression of DHC1 and an ~89% decrease in message levels was observed. Western blots using the DHC1 antibody in N2A cells indicated a >66% decrease in protein levels (5). To test DHC1 antibody specificity in hippocampal culture, cells were transfected on day 9 with DHC1-shRNA with a mCherry marker, and subsequently stained with DHC1 using the established immunofluorescence protocol. Transfection efficiency in hippocampal primary culture is often very low and ~3% of cells successfully received the construct. Transfected cells showed marked decreases in DHC1 staining (Fig. S4 *A*–*D*). Average anti-DHC1 intensity per square micrometer in shRNA transfected cells ($n = 9$) was reduced by 72% compared with control nontransfected cells ($n = 11$) (Fig. S4*E*). The magnitude in signal reduction is analogous to decreases in protein levels assessed by Western blot and confirms reliable specificity of this selected antibody probe.

To validate the KLC1 primary antibody, several approaches were taken. First, to confirm that the KLC1 probe was thoroughly staining its specific target, cells were transfected with a KLC1-mCherry construct after 9 d in culture and probed with the selected anti-KLC1 antibody. The KLC1-mCherry fusion protein produced punctate fluorescence and can be compared with the analogous anti-KLC1 staining. Signal from KLC1-mCherry shows a strong linear correlation ($r = 0.87$) to anti-KLC1 immunofluorescence data (Fig. 2*C* and Fig. S3) and 82.8 ± 1.9% of detected KLC1-mCherry features were found to colocalize with

anti-KLC1 staining. Transfected fluorescently tagged proteins consistently exhibited a slightly higher detection error by Gaussian fitting because of more diffuse patterns of fluorescence compared with antibody staining, thus helping explain the ~17% of KLC1-mCherry features that failed to colocalize with anti-KLC1 puncta within the 300-nm cutoff radius. Second, KLC1 staining in null mice (*KLC1*$^{-/-}$) was determined to directly assess the specificity of the probe (see *Results*). A linear relationship was reported between amount of KLC1 detected with the KLC1 antibody and *KLC1* copy number in Western blots of mouse brain homogenates (5). Of note, hippocampal neurons were costained with antibodies against KLC1 and mitochondrial Cox1 and no significant colocalization between the two markers was observed (5), which is in agreement with reports that mitochondrial transport is independent of KLC1 function (20), and further suggests that the KLC1 antibody was specific.

To shed some light on the proposed cross-reactivity of KLC2 with the KLC1 antibody probe, KLC2 message levels were reduced by transfecting hippocampal neurons with a KLC2-shRNA construct. The vesicular immunofluorescence profiles observed in axons were analyzed after staining of transfected samples. Results indicated minor, yet significant ($P = 0.041$) reductions in overall intensity distributions detected by the KLC1 antibody in KLC2-shRNA transfected cells, suggesting that our antibody probe detected a subset of KLC2 signal. This observation helps explain the absence of a full reduction in KLC1 motor subunit association and intensity in *KLC1*$^{-/-}$ animals. Furthermore, sequence analysis confirmed KLC2 shares a conserved region with KLC1 where the epitope that the V-17 KLC1 antibody recognizes (a proprietary 12- to 20-aa region contained between amino acids 500 and 550). Finally, because *KLC1*$^{-/-}$ animals live to at least embryonic day 19 and in some cases until adulthood, we speculate that KLC2 may take over a portion of the transport of APP vesicles in *KLC1*$^{-/-}$ genotypes. This redundancy of subunits has been previously proposed in mammalian systems (5).

The subpixel colocalization method confirmed that cross-reactivity of secondary antibodies was negligible. When the primary antibody for KLC1 or DHC1 was removed and all other parameters remained unchanged, motor association with APP dropped by 95% and 93% respectively.

Motor Colocalization. To determine motor subunit composition on APP vesicles, a colocalization package was developed and implemented in MATLAB (MathWorks). Subpixel positions of fluorescent point sources from the most in-focus optical slice in each channel were determined by fitting Gaussian functions that approximate the microscope PSF (2, 21). Intensities of puncta were extracted based on the Gaussian amplitude of detected puncta. Colocalization of fluorescent signal between channels was determined using a 300-nm (~2.26 pixels under established imaging conditions) cutoff. For all colocalization data reported, mean percent association was calculated per axon then averaged over all images in the dataset. Accordingly, variability is determined on a per image basis and reported in terms of the SEM in all cases.

The goal of collecting reliable immunofluorescence data were to produce a robust analysis of KLC1 and DHC1 motor content on APP vesicles. Optical microscopes and digital imaging have advanced to the point where recording fluorescent signal from tagged or blotted features has been routine for years. Recently, methods for analyzing these images and for the extraction of quantitative data of the localization and intensity of biological structures have been significantly advanced. Several methods have been reported for automatic detection and localization of puncta (22–27). However, most of these formulations neglect the complex case of partially overlapping, diffraction-limited spots. The punctate features observed in hippocampal axons stained with APP, KLC1, and DHC1 were not in isolation and therefore required additional consideration.

When two tags are separated by a distance smaller than the resolution limit, the superposition of their images gives rise to a single local maximum only. Using a module for multiple spot detection, the problem of unresolved tags was addressed. In each case, a candidate set of mixture models was built and the best candidate model was selected based on pre-established goodness-of-fit criteria (2). The mixture model consists of a superposition of n kernel functions and is formulated, in the case of diffraction-limited spots, as a superposition of n Gaussians, each one representing a version of the PSF shifted in space. Based on simulations and indirect experimental evidence, iterative PSF fitting was found to overcome the diffraction limit by a factor of at least 3; thus, distances of 80–100 nm can be measured without superresolution microscopy (2, 21).

For detection, the most in-focus plane (after registration correction) was extracted for each raw image stack and channel and saved as *.tif. Only raw (nondeconvolved) images were used for analysis because the deconvolution process alters pixel intensity data, and the Gaussian-fitting algorithm itself can be viewed as model-based deconvolution. Candidate frames are user-selected and processed using ImageJ. The user is asked to input the theoretical SD of the PSF (psf σ) for each channel based on the specific wavelength and objective used. The following equation was used to determine psf σ for each channel:

$$\text{psf } \sigma = \frac{0.21 * \left(\frac{\lambda}{\text{N.A.}}\right)}{\text{pixel size}}, \qquad \textbf{[S1]}$$

where λ is the emission wavelength in nanometers, N.A. is the numerical aperture of objective, and pixel size is given in nanometers (2). In reality, the light path is more complicated than what was theoretically assumed, thus the algorithm started with the user-defined theoretical psf σ and subsequently attempted to iteratively estimate a more practical measure based on the raw data. Typically, the practical psf σ calculated was larger than the theoretical one suggested, although—once determined—remained constant during detection of an experimental series. Finally, α-values for detection statistics and initial local maxima assessment are determined by the user.

Once settings are established, the algorithm scans a given image and marks intensity maxima positions (brightest pixel within a detected point source) after local background assessment for each punctate feature. Then, the algorithm iteratively attempts to fit one or more Gaussian functions to the area surrounding a local maxima "seed." Position information was achieved at subpixel resolution because the 2D fitting algorithm accounts for all local intensity information. Once a Gaussian was successfully fit, an estimated measure of point-source intensity based on the Gaussian amplitude was returned to the user (21). Because the SD (σ) of Gaussians used was held constant for each channel and experimental series, relative intensity levels can be directly compared with achieve reliable readouts of fluorophore amount.

Before colocalization analysis, intensity thresholds were determined to filter unwanted immunofluorescence signal (noise). Secondary-only control images were collected for each experimental dataset and provided a measure of background fluorescence from Alexa Fluor probes within axonal projections. Dynamic range of background intensity for each channel was established in these control images and used to threshold detected features from experimental images by removing detected puncta for each antibody probe with intensities less than what was described by 95% of background range.

Immunofluorescence images are notorious for containing staining artifacts. Although every possible measure was taken to

reduce staining noise in acquired datasets, selected axonal projections were not entirely free of artifacts. Immunofluorescence artifacts typically manifest themselves as bright, large "blobs" that can be distinguished from true signal. These blobs are filtered by taking all intensity measurements for a given region and sorting them from largest to smallest. Staining artifacts generally have intensities greater than $\mu + 3\sigma$ of detected features, and are traced back to raw images for manual inspection. An appropriate cutoff was determined based on these criteria and used for analysis of each experimental series.

In the motor colocalization code output, four APP vesicle categories were designated: those that had KLC1 only, DHC1 only, both motor subunits, or no motor subunits associated within a 300-nm radius of an APP point source. The motor localization function output was divided into several sections. First, the subpixel localization coordinates and associated intensity amplitude of each APP vesicle were listed, followed by a readout that places it into its designated category. Next, a summary of percent motor association for all vesicles detected was returned. Third, each KLC1 "hit"—KLC1 point source associated within 300 nm of an APP vesicle—was listed, including subpixel position, intensity, distance from associated APP, and associated APP intensity. An analogous list for DHC1 is subsequently provided. Finally, position and intensity measurements are accompanied by an associated error interval or goodness-of-fit, respectively (2, 21). Computational expense and running time was minimal for large datasets.

Mode Clustering. Intensity amplitudes of APP vesicles and KLC1 and DHC1 motor subunits were nonnormal and clustered using the MCLUST package in R statistical computing environment (28). Optimal fits were selected using Bayesian Information Criterion, permitting robust statistical comparison of models with differing clusters. Regardless of the number of bins used to display the resulting distributions, clustering results remained constant. Classification of intensity values to a specific mode was done after calculating threshold values for the intersection of two Gaussian functions (29).

Statistics. Statistical significance was determined using both parametric and nonparametric tests. Normality for each dataset obtained in this study was assessed using the Anderson Darling and Lilliefors statistical tests. We determined that samples in a population were not normally distributed when $P < 0.05$. A two-tailed Student t test was used for comparison between normally distributed populations. Most parameters were not normally distributed, so a nonparametric permutation t test was used (29). For all tests used, P values < 0.05 were considered significant.

1. Bobroff N (1986) Position measurement with a resolution and noise-limited instrument. *Rev Sci Instrum* 57:1152–1157.
2. Thomann D, Rines DR, Sorger PK, Danuser G (2002) Automatic fluorescent tag detection in 3D with super-resolution: Application to the analysis of chromosome movement. *J Microsc* 208:49–64.
3. Brady ST, Pfister KK, Bloom GS (1990) A monoclonal antibody against kinesin inhibits both anterograde and retrograde fast axonal transport in squid axoplasm. *Proc Natl Acad Sci USA* 87:1061–1065.
4. Pilling AD, Horiuchi D, Lively CM, Saxton WM (2006) Kinesin-1 and Dynein are the primary motors for fast transport of mitochondria in *Drosophila* motor axons. *Mol Biol Cell* 17:2057–2068.
5. Encalada SE, Szpankowski L, Xia CH, Goldstein LS (2011) Stable kinesin and dynein assemblies drive the axonal transport of mammalian prion protein vesicles. *Cell* 144:551–565.
6. Colin E, et al. (2008) Huntingtin phosphorylation acts as a molecular switch for anterograde/retrograde transport in neurons. *EMBO J* 27:2124–2134.
7. Martin M, et al. (1999) Cytoplasmic dynein, the dynactin complex, and kinesin are interdependent and essential for fast axonal transport. *Mol Biol Cell* 10:3717–3728.
8. Reis GF, et al. (2012) Molecular motor function in axonal transport in vivo probed by genetic and computational analysis in *Drosophila*. *Mol Biol Cell*, 10.1091/mbc.E11-11-0938.
9. Gunawardena S, Goldstein LS (2001) Disruption of axonal transport and neuronal viability by amyloid precursor protein mutations in *Drosophila*. *Neuron* 32:389–401.
10. Shubeita GT, et al. (2008) Consequences of motor copy number on the intracellular transport of kinesin-1-driven lipid droplets. *Cell* 135:1098–1107.
11. Rock RS (2010) Intracellular transport: Force controls motor switching at filament junctions. *Curr Biol* 20:R525–R527.
12. Muresan Z, Muresan V (2005) Coordinated transport of phosphorylated amyloid-beta precursor protein and c-Jun NH2-terminal kinase-interacting protein-1. *J Cell Biol* 171:615–625.
13. Muresan V, Varvel NH, Lamb BT, Muresan Z (2009) The cleavage products of amyloid-beta precursor protein are sorted to distinct carrier vesicles that are independently transported within neurites. *J Neurosci* 29:3565–3578.
14. Rahman A, Kamal A, Roberts EA, Goldstein LS (1999) Defective kinesin heavy chain behavior in mouse kinesin light chain mutants. *J Cell Biol* 146:1277–1288.
15. Zheng H, et al. (1995) beta-Amyloid precursor protein-deficient mice show reactive gliosis and decreased locomotor activity. *Cell* 81:525–531.
16. Falzone TL, et al. (2009) Axonal stress kinase activation and tau misbehavior induced by kinesin-1 transport defects. *J Neurosci* 29:5758–5767.
17. Kaether C, Skehel P, Dotti CG (2000) Axonal membrane proteins are transported in distinct carriers: A two-color video microscopy study in cultured hippocampal neurons. *Mol Biol Cell* 11:1213–1224.
18. Geng J, Baba M, Nair U, Klionsky DJ (2008) Quantitative analysis of autophagy-related protein stoichiometry by fluorescence microscopy. *J Cell Biol* 182:129–140.
19. Souchier C, Brisson C, Batteux B, Robert-Nicoud M, Bryon PA (2003) Data reproducibility in fluorescence image analysis. *Methods Cell Sci* 25:195–200.
20. Glater EE, Megeath LJ, Stowers RS, Schwarz TL (2006) Axonal transport of mitochondria requires milton to recruit kinesin heavy chain and is light chain independent. *J Cell Biol* 173:545–557.
21. Jaqaman K, et al. (2008) Robust single-particle tracking in live-cell time-lapse sequences. *Nat Methods* 5:695–702.
22. Anthony SM, Granick S (2009) Image analysis with rapid and accurate two-dimensional Gaussian fitting. *Langmuir* 25:8152–8160.
23. Bornfleth H, Edelmann P, Zink D, Cremer T, Cremer C (1999) Quantitative motion analysis of subchromosomal foci in living cells using four-dimensional microscopy. *Biophys J* 77:2871–2886.
24. Cheezum MK, Walker WF, Guilford WH (2001) Quantitative comparison of algorithms for tracking single fluorescent particles. *Biophys J* 81:2378–2388.
25. Goulian M, Simon SM (2000) Tracking single proteins within cells. *Biophys J* 79:2188–2198.
26. Kubitscheck U, Kückmann O, Kues T, Peters R (2000) Imaging and tracking of single GFP molecules in solution. *Biophys J* 78:2170–2179.
27. Netten H, et al. (1997) FISH and chips: Automation of fluorescent dot counting in interphase cell nuclei. *Cytometry* 28:1–10.
28. Fraley C, Raftery AE (1999) MCLUST: Software for model based cluster analysis. *J. Classification* 16:297–306.
29. Moore DS, McCabe GP (2005) *Introduction to the Practice of Statistics* (W.H. Freeman, New York), 5th Ed.

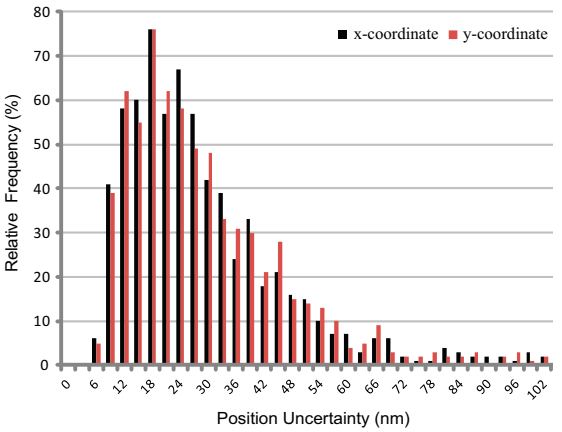

Fig. S1. Observed uncertainty in feature position estimation for APP in WT axons. Mean position uncertainty in *x* and *y* is 29.6 nm and 29.9 nm, respectively. Of note, 92.6% of the position data had an error of less than 60 nm. $n_{Vesicles}$ = 705, $n_{Animals}$ = 6, n_{Axons} = 6.

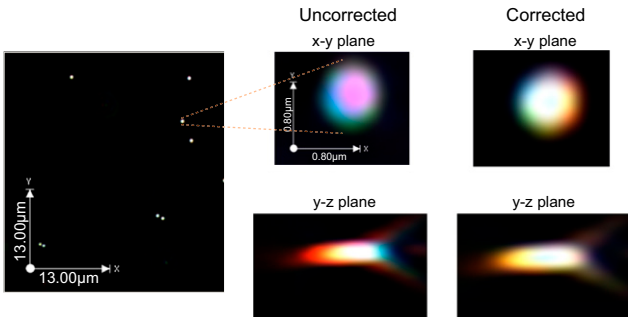

Fig. S2. Registration correction. FITC, Cy-5, Tx-Rd channel alignment using TetraSpeck microspheres. (*Left*) A portion of a raw bead image acquired using a 100× 1.4 NA objective on the RT DeltaVision Deconvolution system. (*Center*) A zoomed uncorrected (raw) single bead in both the *x-y* and *y-z* planes. Pixel registration correction indicates a +1 optical slice upward shift in A568 is sufficient to align signal and account for aberration. (A488: anchor; A647: $x = 0$, $y = 0$, $z = 0$; A568: $x = 0$, $y = 0$, $z = +1$). (*Right*) Microsphere in *x-y* and *y-z* planes after correction.

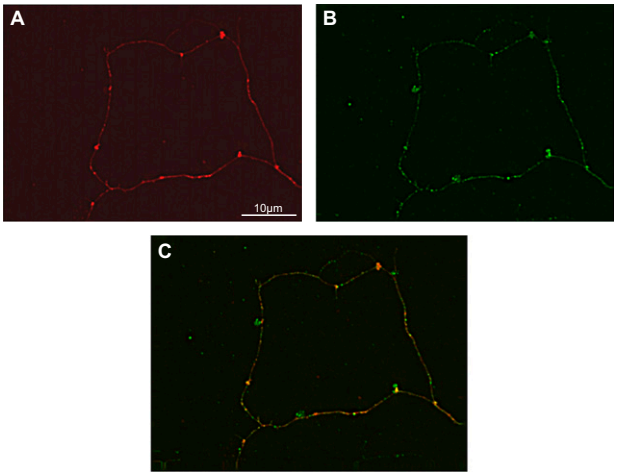

Fig. S3. Validating KLC1 antibody specificity. (*A*) KLC1-mCherry transfected hippocampal axon. (*B*) Anti-KLC1 staining. (*C*) Merge. All images at 100×.

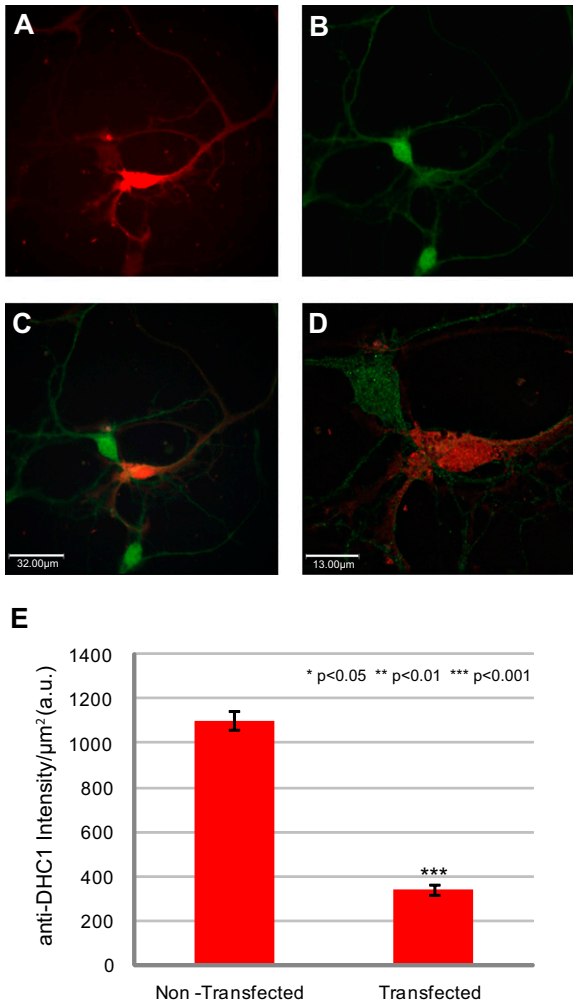

Fig. S4. Validating DHC1 antibody specificity. (*A*) A 40× image showing three hippocampal cells, one of which (middle of image) was transfected with DHC1-shRNA-mCherry. (*B*) Anti-DHC staining at 40×. (*C*) Merge at 40×. (*D*) Merge at 100×. (*E*) Quantification of intensity per micrometer decrease in transfected cells (n_{cells} = 9) vs. nontransfected cells (n_{cells} = 11). Error bars show SEM.

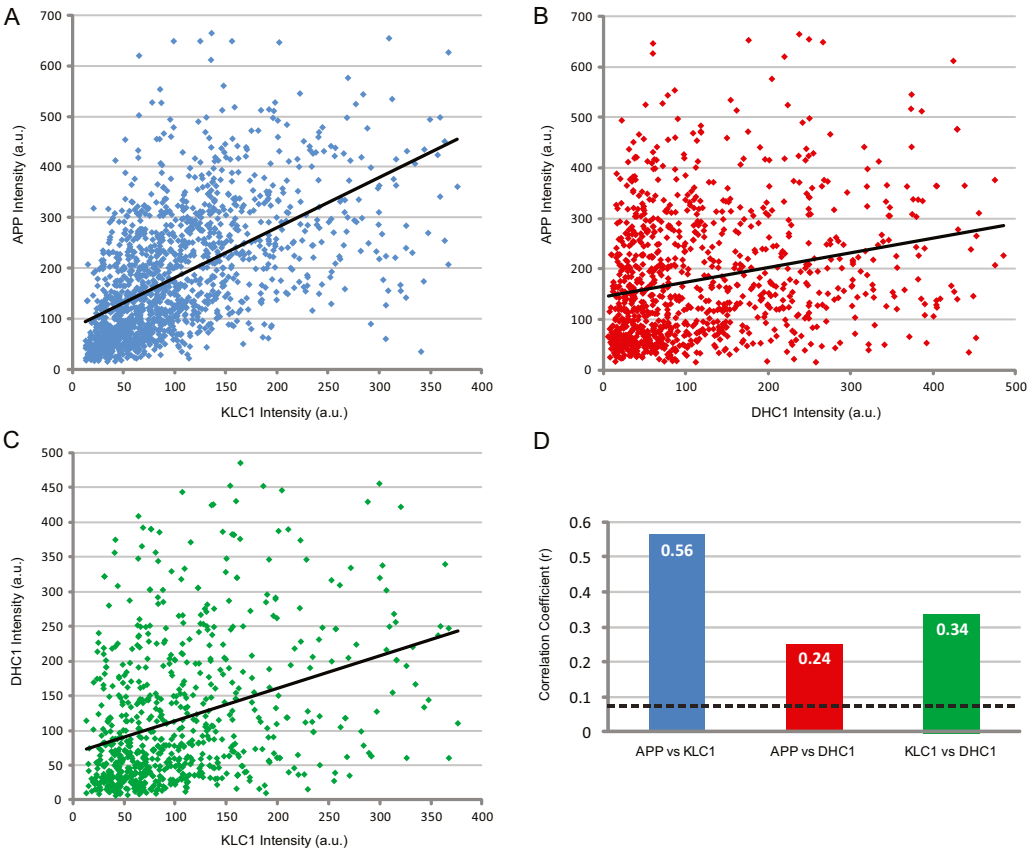

Fig. S5. Motor subunit intensity correlation in WT axons. (*A*) Scatterplot of KLC1 vs. APP for all APP vesicle-associated KLC1 intensities. $n_{Vesicles}$ = 1,515. (*B*) Scatterplot of DHC1 vs. APP for all APP vesicle-associated DHC1 intensities. $n_{Vesicles}$ = 1,014. (*C*) Scatterplot of KLC1 vs. DHC1 intensity for all APP vesicles associated with both subunits. $n_{Vesicles}$ = 757. (*D*) Coefficients of correlation for each pair of intensity measures in *A*–*C*. To determine statistical significance for coefficients of correlation between motor subunit and APP intensities combinations, we first obtained 10,000 bootstrap replicates of each correlation coefficient to reveal its distribution. We subsequently calculated the maximal (3σ) range of correlation coefficients under random pairings for each intensity comparison (indicated by the black horizontal bar). Of note, these significant correlations are not the result of bleed-through between channels during image acquisition, as each fluorescent channel was imaged separately using filters that avoid crosstalk, and selected secondary Alexa fluorophores are well separated, resulting in minimal spectral overlap.

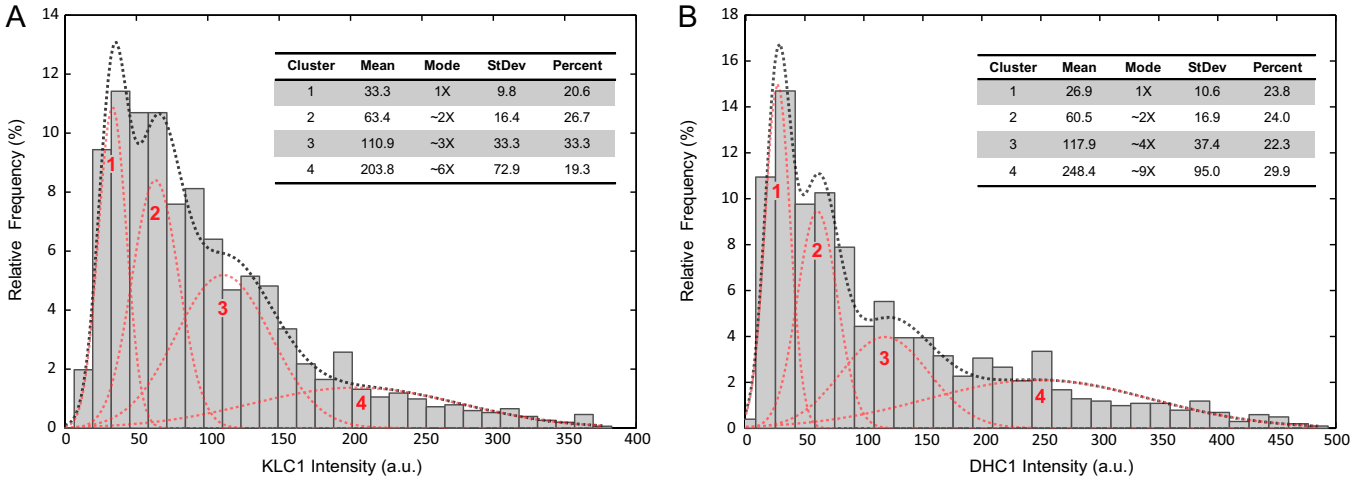

Fig. S6. APP-associated motor subunit intensity clustering in WT axons. (*A*) KLC1. $n_{Vesicles}$ = 1,515, $n_{Animals}$ = 3, n_{Axons} = 17. (*B*) DHC1. $n_{Vesicles}$ = 1,014, $n_{Animals}$ = 3, n_{Axons} = 17. In both cases, bin number = 30.

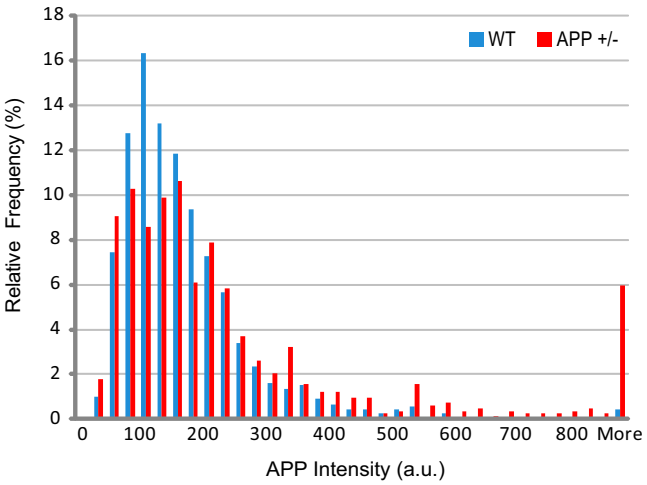

Fig. S7. APP intensity profile in WT vs. *APP*$^{+/-}$ animals. Bin size = 25 AU. For *A* and *B*: WT: $n_{Vesicles}$ = 4,050, $n_{Animals}$ = 6, n_{Axons} = 34; *APP*$^{+/-}$: $n_{Vesicles}$ = 1,511, $n_{Animals}$ = 6, n_{Axons} = 20.

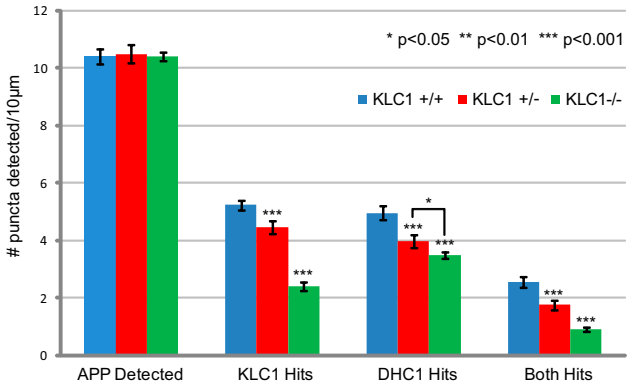

Fig. S8. Number of features detected per 10 µm in *KLC1* genotypes. *KLC1*$^{+/+}$: $n_{Vesicles}$ = 1,676, $n_{Animals}$ = 4, n_{Axons} = 20; *KLC1*$^{+/-}$: $n_{Vesicles}$ = 1,760, $n_{Animals}$ = 4, n_{Axons} = 19; *KLC1*$^{-/-}$: $n_{Vesicles}$ = 1,569, $n_{Animals}$ = 3, n_{Axons} = 17. Error bars show SEM.